Melt flow instability in laser metal additive manufacturing

Qilin Guo[1, 2], Minglei Qu[1, 2], Luis I. Escano[1], S. Mohammad H. Hojjatzadeh[1, 2], Zachary Young[1], Kamel Fezzaa[3], Lianyi Chen[1, 2, *]

[1]Department of Mechanical Engineering, University of Wisconsin-Madison, Madison, Wisconsin 53706, USA

[2]Department of Materials Science and Engineering, University of Wisconsin-Madison, Madison, Wisconsin 53706, USA

[3]X-ray Science Division, Argonne National Laboratory, Lemont, Illinois 60439, USA

*Corresponding author: lianyi.chen@wisc.edu

Corresponding author address: 1035 Mechanical Engineering Building, 1513 University Avenue, Madison, Wisconsin 53706, USA.

Acknowledgements

This work is supported by US National Science Foundation. This research used resources of the Advanced Photon Source, a U.S. Department of Energy (DOE) Office of Science User Facility operated for the DOE Office of Science by Argonne National Laboratory under Contract No. DE-AC02-06CH11357.

CRediT author statement

Qilin Guo: Conceptualization, Formal analysis, Investigation, Methodology, Writing – original draft, Writing – review & editing. **Minglei Qu:** Investigation, Methodology, Validation. **Luis I. Escano:** Investigation. **S. Mohammad H. Hojjatzadeh:** Investigation. **Zachary Young:** Investigation. **Kamel Fezzaa:** Methodology, Resources. **Lianyi Chen:** Conceptualization, Funding acquisition, Investigation, Methodology, Project administration, Resources, Writing – review & editing.

Declaration of interest

The authors declare no competing interests.

Revealing melt flow instabilities in laser powder bed fusion additive manufacturing of aluminum alloy via in-situ high-speed X-ray imaging

Abstract

Laser metal additive manufacturing technologies enable the fabrication of geometrically and compositionally complex parts unachievable by conventional manufacturing methods. However, the certification and qualification of additively manufactured parts are greatly hindered by the stochastic melt flow instabilities intrinsic to the process, which has not been explicitly revealed by direct observation. Here, we report the mechanisms of the melt flow instabilities in laser powder bed fusion additive manufacturing process revealed by in-situ high-speed high-resolution synchrotron X-ray imaging. We identified powder/droplet impact, significant keyhole oscillation, and melting-mode switching as three major mechanisms for causing melt flow instabilities. We demonstrated the detrimental consequences of these instabilities brought to the process, and projected new understanding on the melt flow evolution and keyhole oscillation. This work provides critical insights into process instabilities during laser metal additive manufacturing, which may guide the development of instability mitigation approaches. The results reported here are also important for the development and validation of high-fidelity computational models.

Keywords

Additive manufacturing, laser processing, melt flow, synchrotron X-ray imaging

1. Introduction

Laser metal additive manufacturing technologies have the potential to revolutionize manufacturing industry by enabling the fabrication of geometrically and compositionally complex parts unachievable by conventional manufacturing methods [1–3]. To fabricate parts with desirable and predictable quality, extensive research have dedicated to correlate the process dynamics (melt pool variation [4,5], pore formation [6–8], spatter generation [9,10], keyhole oscillation [11–13], etc.) with the processing conditions (laser power, scan speed, beam size, etc.), in an effort to establish an "optimized" set of parameters to produce parts with less defects and higher density [14–17]. However, there are uncertainties intrinsic to the laser metal additive manufacturing process where some unstable physical dynamics are not tightly bonded to specific processing conditions [16–20]. Such instabilities pose great uncertainty to the qualification and certification of the additively manufactured parts [20–22], which require explicit characterization through direct observations.

To investigate the process instabilities, it is essential to trace the transient melt flow behavior inside the melt pool—the direct product of laser-matter interaction. However, the opacity of metals to visible light poses great barrier in direct observation of the molten metals within the melt pools. To overcome this challenge, recent research has applied synchrotron radiation based in-situ X-ray imaging to observe the physical dynamics within metals [5,6,10,23–26]. By in-situ X-ray imaging, the localized melt flow behavior within a laser induced metallic melt pool could be inferred from the movement of pores generated during the process [5,26,27]. The regular melt flow patterns within the whole melt pool have also been studied using tungsten particles as flow tracers [6,23–25].

Limited research has been conducted toward experimental investigations on melt flow instabilities. In blown powder directed energy deposition (DED) additive manufacturing process, it was reported that the impact of feeding particles can cause melt pool surface fluctuations, generate porosity, and cause keyhole oscillations [26]. In laser powder bed fusion (LPBF) additive manufacturing process, it was reported that high laser scan speeds and large powder layer thickness can cause unstable melt flow, which could lead to rough surface finish [28]. The melt flow behavior was inferred by the morphology of solidified track, as well as the powder spattering behavior. Recent research using in-situ X-ray imaging to monitor the LPBF process has reported several defect-formation mechanisms resulting from unstable melt flow behavior or depression zone fluctuations, although the unstable melt flow behavior itself was not characterized [29].

Computational modeling work has also been performed to study the melt flow instabilities. In general, the studies focused on two aspects: the instability formation mechanism and the consequences of the instabilities on the process. Surface tension variation was identified as a source of melt flow instabilities, as surface tension is one of the major driving forces for liquid migration. The surface tension fluctuations could be induced by both improper processing parameters (such as hatch spacing [30]) and chemical composition variations (such as increased oxidation level [31]) . The inhomogeneous powder packing in the LPBF powder bed also serves as a source to disturb the melt flow by cutting off the liquid migration at the loose-packing region, resulting in part defects such as porosity and balling [32]. As for the consequences, the melt flow instabilities have been reported to be accountable for the breakup of melt tracks (Plateau-Rayleigh instability), trap of gas pores, and creating denudation zone around the keyhole rim during LPBF [33]. Other melt flow induced process instabilities such as liquid ejection and periodical oscillations of keyhole have also been demonstrated by high-fidelity simulations [11,34,35].

So far, in-process experimental characterization of the melt flow instabilities during LPBF has not been reported. In the present work, we report the melt flow instabilities within aluminum melt pools during laser powder bed fusion process revealed by in-situ high-speed, high-energy, high-resolution synchrotron X-ray imaging with uniformly dispersed populous micro-tracers. We investigate the mechanisms for causing three major types of melt flow instabilities and quantify the influence of these instabilities in both local scale and global scale. We also demonstrate the detrimental consequences that the instabilities exert to the process. Inspired by the results, we further elaborate our new understandings on the mechanisms of keyhole oscillation and melt flow evolution.

2. Methods and Materials

2.1 In-situ laser melting X-ray imaging experiment

We used in-situ laser-melting X-ray imaging to monitor the dynamics of melt flow inside the melt pool during laser melting/scanning on an aluminum powder bed, as schematically illustrated in Fig. 1(a). The powder bed was composed of a metal substrate (0.5 mm thick along X-ray transmission direction), a manually-spread powder layer with 100 μm thickness, and two glassy carbon walls for holding the powder. A vertical Gaussian laser beam with a $1/e^2$ diameter of ~100 μm scans the powder bed to create a moving melt pool. The laser is a 1070 nm wavelength, continuous-wave, single-mode, ytterbium fiber laser (YLR-500-AC, IPG Photonics, USA), positioned by a galvo scan head (IntelliSCAN$_{de}$ 30, SCANLAB GmbH, Germany). During laser scanning, a stationary high-energy synchrotron X-ray beam (at beamline 32-ID of Argonne National Laboratory's Advanced Photon Source) penetrated through the specimen from horizontal direction. The transmitted X-ray beam carrying melt flow information was converted by a scintillator (LuAG:Ce) into visible light, which was recorded by a high-speed camera with a frame rate of either 140 kHz or 50 kHz, and a spatial resolution of 1.97 μm per pixel. Therefore, all the physical dynamics were projected on a 2D imaging plane. Aluminum alloy feedstock powder (AlSi10Mg and Al6061) were uniformly mixed with 1 vol.% flow tracers (5 μm tungsten particles) by ball milling to trace the melt flow, as schematically illustrated in Fig. 1(b). The powder size distribution of aluminum feedstocks after ball milling is shown in Fig. 1(c).

2.2 Materials

Two aluminum alloys were used in this work: AlSi10Mg and Al-6061. Aluminum alloys were chosen for their high X-ray transparency. AlSi10Mg alloy, as one of the most widely used alloy in additive manufacturing, has enhanced laser absorption by the enriched Si content [36]. Therefore, AlSi10Mg was used in this work to study the melt flow in relatively large melt pools (keyhole-mode and transition-mode). Al-6061, as a common aluminum alloy on market, has low laser absorptivity. It was used to investigate the dynamics in conduction-mode melt pool or the incidents that are sensitive to laser absorption.

The alloy substrates with dimensions of 40 mm × 3 mm ×0.5 mm for in-situ X-ray imaging were prepared by wire electrical discharge machining (wire EDM). The dimension along X-ray incidence is 0.5 mm to ensure better X-ray transparency. The surface of the substrate was ground by 400-grit sand paper to remove any contaminations. The aluminum powders were uniformly mixed with 1 vol.% tungsten micro-particles (5 μm) as flow tracers by ball milling.

2.3 Surface morphology characterization

Scanning electron microscopy (SEM) was performed on a Zeiss LEO-1530 field emission scanning electron microscope to observe the solidified track surface morphology. The sample was pre-tilted to 60° with respect to the electron beam for better observation of the track height.

The surface profiles of the solidified track were measured on a VHX-5000 Digital Microscope (KEYENCE Corporation of America).

2.4 Melt flow tracing approach

The speed (v) of a tungsten tracer was calculated by dividing its displacement (d) by its traveling time (t), v = d/t. The tracer's displacement (d) was calculated via its two-dimensional (2D) coordinates change ($\Delta x = |x_2 - x_1|$, $\Delta y = |y_2 - y_1|$) from one frame to the next frame in the 2D X-ray image planes, where $d = (\Delta x^2 + \Delta y^2)^{1/2}$. The tungsten tracer's travelling time (t) is the time interval between two frames, determined by the recording frame rate of the X-ray imaging video (50 kHz or 140 kHz in the present work).

To examine whether adding 1 vol.% tungsten particles to aluminum powder bed could change the laser absorption behavior, we conducted two laser-melting experiments using different powder beds but identical laser processing conditions (364 W, 0.5 m/s). The results are displayed in Fig. 2. As shown in Fig. 2(a), AlSi10Mg powder mixed with 1 vol.% tungsten particles generated a keyhole (laser induced vapor cavity) depth of 200 ± 24 μm (averaged over 100 frames). The keyhole generated with pure AlSi10Mg powder bed exhibited an average depth of 197 ± 31 μm, as shown in Fig. 2(b), which is only 1.5% smaller than the keyhole depth generated with mixed powder bed. Therefore, the influence of 1 vol.% tungsten on laser absorption is minimal.

In addition to the laser absorption, it has also been reported that adding 1 vol.% of tungsten particles to the aluminum feedstock does not have significant impact on the physical property of the aluminum melt pool [23]. Thus, it is feasible to use tungsten microparticles as flow tracers.

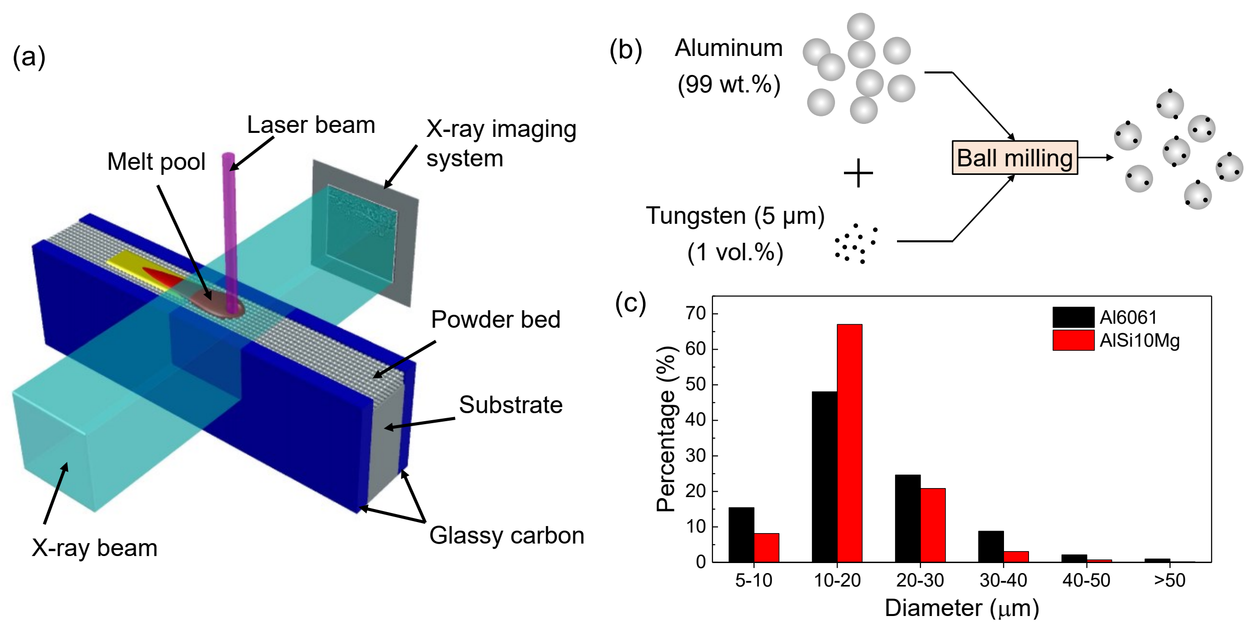

Fig. 1. Method for in-situ melt flow mapping experiment. *(a) Schematic illustration of the experiment setup for X-ray imaging of laser powder bed fusion process. (b) Powder preparation method for melt flow tracing. The feedstock aluminum powder was mixed with 1 vol.% tungsten particles by ball milling. (c) Aluminum particle size distributions of the feedstock Al6061 and AlSi10Mg powder after ball milling with tungsten particles. The distribution calculation did not include aluminum particles smaller than 5 μm or tungsten particles.*

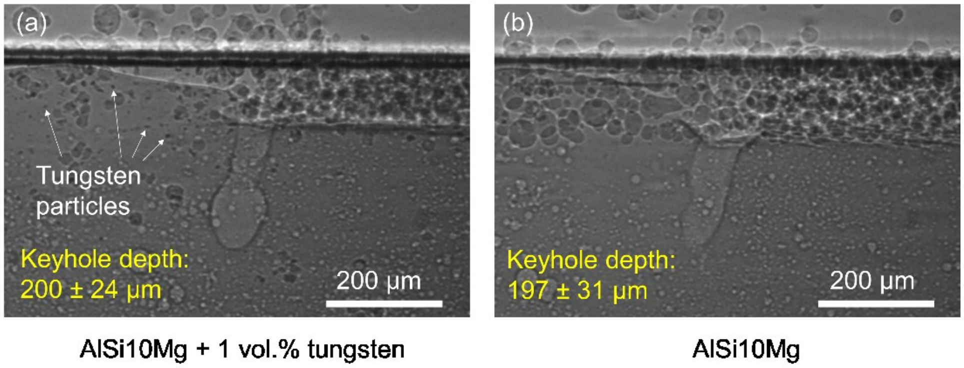

Fig. 2. Comparison of keyhole depth during laser melting of AlSi10Mg + 1 vol.% tungsten mixed powder and pure AlSi10Mg powder. *The laser processing conditions are identical for the two experiments: 364 W laser power, 0.5 m/s scan speed.*

2.5 Definition of laser melting modes

The laser power and scan speed were varied to realize three major melting modes during the investigation of melt flow instabilities, including keyhole mode, conduction mode, and transition mode. There are two major approaches to distinguish different melting modes.

One of the approaches is based on physics [37,38]: Keyhole-mode melting is dominated by convective heat transfer, conduction-mode melting is dominated by heat conduction; while transition-mode melting is in between of the keyhole mode and conduction mode.

The other classification approach is based on geometry [4]: A keyhole-mode melt pool contains large melt volume with a deep depression zone induced by intensive vaporization of materials. The aspect ratio (W/2)/D (half width over depth) of the depression zone is usually less than 1. A conduction-mode melt pool forms under low laser radiation, thus contains small melt volume without having a depression zone. A transition-mode melt pool is created under conditions between keyhole-mode and conduction-mode laser melting, with a slightly larger (or similar) melt volume than conduction-mode melt pool, yet still holds a depression zone with an aspect ratio of $(W/2)/D > 1$. In the present work, we took the second approach to define the laser melting modes.

3. Results

We identified three major mechanisms for causing melt flow instabilities during laser processing, i.e., powder/droplet impact, significant keyhole oscillation, and melting-mode switching. The influences of these instabilities on the melt flow behavior are demonstrated below.

3.1 Powder/droplet impact induced melt flow instability

The flowable powder, as the core and unique element in the dominating powder-based laser metal additive manufacturing technologies, enables great flexibility for process design, but also brings frequent disturbances to the process [13]. Herein, we report two types of melt flow instabilities induced by the powder.

3.1.1 Local instability induced by powder/droplet impact

In laser metal additive manufacturing process, a laser-driven proceeding melt pool continuously captures the powder on the powder bed to grow into a part. However, the incorporating powder can be large in size (more than three times larger than the feedstock powder), due to agglomerations or merging of small droplets. The impact of large powder clusters or droplets into a melt pool with large melt volume (i.e. keyhole-mode melt pool) could locally disturb the regular melt flow pattern, as elucidated in Fig. 3 (and Supplementary Video 1).

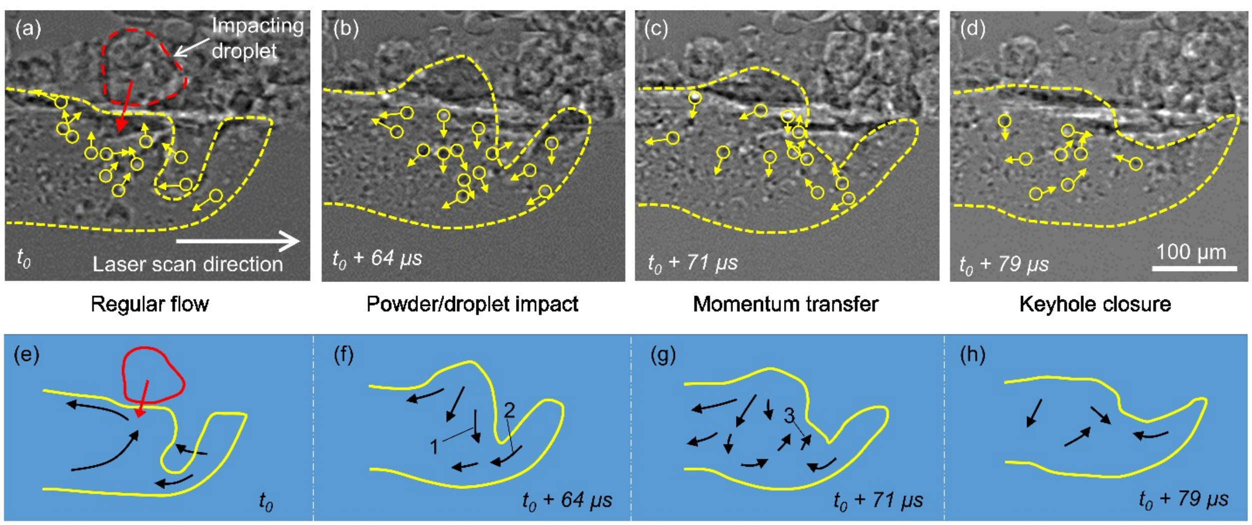

Fig. 3. Powder/droplet impact induced local melt flow instability. *(a–d) X-ray images showing the melt flow change during a droplet impacting to keyhole-mode melt pool. The laser power is 312 W with a scan speed of 0.6 m/s. The material is AlSi10Mg. (e–h) Schematic illustration of the melt flow change in (a–d).*

Figure 3(a–d) display X-ray images where a melt pool moves from left to right in the field of view. Yellow dashed lines marked the melt pool boundaries. The laser is invisible in the view, whereas its location was indicated by the moving keyhole. The flow tracers were circled with arrows pointing out their instant moving directions. By connecting the movements of individual tracers, the melt flow patterns were deducted and schematically exhibited in Fig. 3(e–h).

During an impact, the droplet transfers kinetic energy and potential energy into the melt pool, locally altering the original flow direction (Fig. 3(a,e)) into the droplet momentum direction (Fig. 3(b,f)) at the impact location. The collision between foreign flow (carrying liquid from the droplet) and the original flow (carrying liquid from the melt pool) exhausted the impact energy and dampened the droplet impact from spreading further. The downward flows 1 and 2 (Fig. 3(f)) collided at the keyhole bottom and formed an upward flow 3 (Fig. 3(g)), pushing the keyhole bottom surface upward till the depression almost vanished (Fig. 3(d,h)). Although keyhole vanishing is momentary, it can reduce the local laser absorption and cause undesired energy fluctuation in the process [4].

3.1.2 Global instability induced by powder/droplet impact

Compared with the above keyhole-mode laser melt pool, a conduction-mode laser melt pool contains much less liquid volume, which cannot efficiently dampen and confine the powder/droplet impact within a local region. Rather, the melt flow instability brought by the impact on conduction-mode melt pool is global and more detrimental, as demonstrated in Fig. 4.

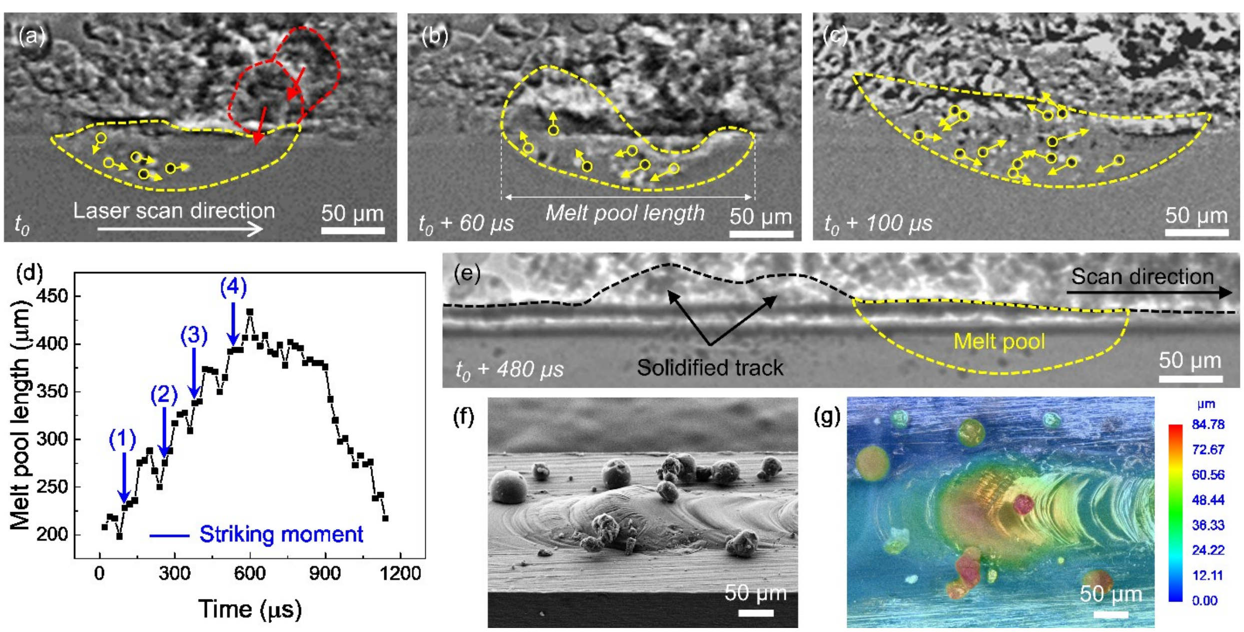

Fig. 4. Powder/droplet impact induced global melt flow instability. *(a–c) X-ray images showing the melt flow change during a droplet impacting to conduction-mode melt pool. The laser power*

is 312 W with a scan speed of 0.6 m/s. The material is Al6061. (d) Effect of droplet striking on the melt pool length development as a function of time. (e) X-ray image showing the profile of the solidified melt track resulting from droplet impact. (f) SEM image showing the solidified track at the same region as in (e). (g) Surface profile of the solidified track at the same imaging area as in (e) and (f).

During an impact, as shown in Fig. 4(a), two droplets together carrying a liquid volume nearly one-third of a conduction-mode melt pool struck on the front melt pool surface. The impact broke the original regular flow pattern in the whole melt pool, as evidenced by the reversed flow direction at the rear-bottom of melt pool, which changed from moving forward (Fig. 4(a)) to backward (Fig. 4(b)). The surface level at the rear melt pool was kicked up by the striking (Fig. 4(b)) and rapidly solidified as it is (Fig. 4(e,f)), adding up to the surface roughness of the as-printed layer. Surface profiling measurement in Fig. 4(g) shows the elevated track height can be 50 μm-higher than the average solidified track height. The impact droplet also increases the volume of liquid metal in the melt pool, leading to the melt pool elongation, as shown in Fig. 4(c).

Large powder/droplet impact is not an occasional event in laser metal additive manufacturing process. We quantified the striking incidence by evaluating the melt pool length change in 1200 μs during laser scanning, as shown in Fig. 4(d). Within the first 600 μs, we observed four striking events, leading to a continuous elongation of the melt pool from ~200 μm to 434 μm (over 100% increase). We noticed that the droplet-striking event did not elongate the melt pool immediately. The elongation usually occurs 20-60 μs after the striking, because the striking liquid takes time to travel along the melt pool. No striking event happened for the remaining 600 μs (from 600 μs to 1200 μs in Fig. 4(d)), during which the melt pool length gradually recovered to the original size. This result demonstrates that the powder/droplet striking occurs frequently and randomly during laser scanning, which brings uncertainty to the qualification of additively manufactured parts.

3.2 Significant keyhole oscillation induced melt flow instability

3.2.1 Local instability induced by significant keyhole oscillation

The melt flow patterns around the keyhole are highly dependent on the keyhole behavior. A significant keyhole oscillation with an amplitude over twice as large as the original keyhole size can override the original flow patterns at adjacent areas.

When a significant keyhole oscillation happens, the liquid at the rear keyhole wall was pushed backward to form a surface wave, as shown by the X-ray images in Fig. 5(a,b) and the schematic illustrations in Fig. 5(e,f). The wave front I (Fig. 5(f)) squeezed the rear rim of the keyhole to generate a protruding surface wave, which propagated backward against the laser scanning direction. Aside from the main surface wave (as shown in Fig. 5(b)), a secondary wave possibly locating at the side of the melt track formed afterward, as displayed in Fig. 5(c) and Supplementary Fig. 1. The possible configuration that could cause overlaying contrast in X-ray images is demonstrated in Supplementary Fig. 2. The liquid beneath the surface wave got compressed and spread away to a broader area with a speed of ~0.6 m/s (measured by tracing the displacement of wave front II in Fig. 5(g,h)). With the spreading of compressed wave, the liquid metal at the affected area moved along the wave propagating direction temporarily, while the original flow pattern was temporarily erased and overridden.

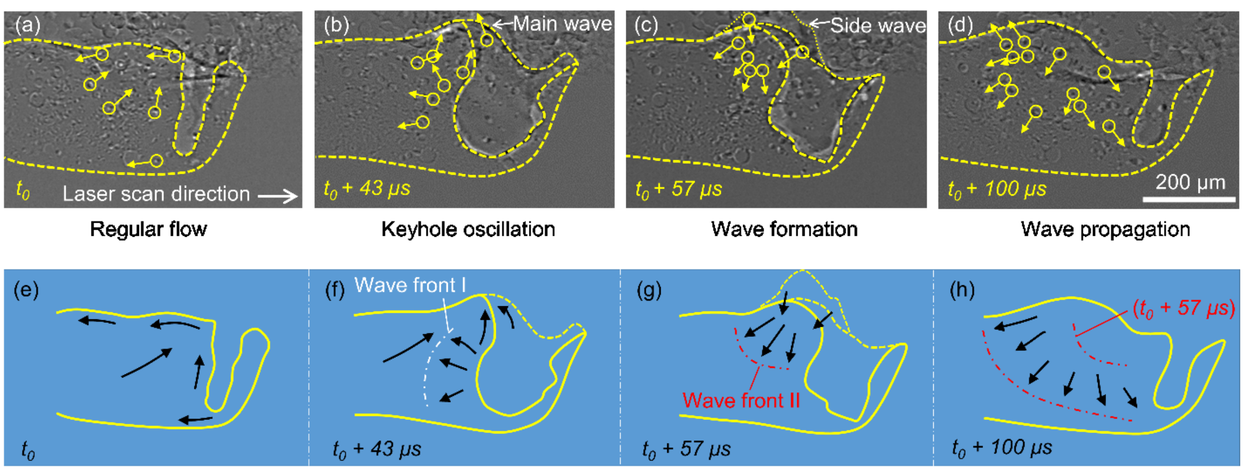

Fig. 5. Significant keyhole oscillation induced local melt flow instability. *(a–d) X-ray images showing the melt flow change during a significant keyhole oscillation event. The laser power is 364 W with a scan speed of 0.6 m/s. The material is AlSi10Mg. (e–h) Schematic illustration of the melt flow change in (a–d).*

3.2.2 Global instability induced by significant keyhole oscillation

A global effect takes place when a significant keyhole oscillation occurs in a moderate-size keyhole-mode melt pool or a transition-mode melt pool, as shown by Fig. 6. Initially, the oscillation created a backward-moving wave that compressed the liquid behind the keyhole, as shown in Fig. 6(b,e), which is similar to the event in Fig. 5. However, different from Fig. 5, the compressed liquid did not spread far before it touched the bottom of the shallow melt pool, where the liquid split into two flows (Fig. 6(c,f)): flow-1, moving backward to the rear melt pool; and flow-2, moving forward to the front melt pool. The splitting flows initiated a series of instabilities to the process, as demonstrated in Fig. 6(g–i):

(1) Reduction of solidification rate occurred at the tail of the melt pool, as indicated by the red arrow in Fig. 6h. Under regular melt flow patterns, as shown in Fig. 6(a)), the solid-liquid interface at the melt pool bottom was smooth and convex. However, the significant keyhole oscillation pushed a large volume of liquid moving backward to the rear melt pool, slowing down the solidification at the rear bottom of the melt pool. As a result, a concave was observed on the solid-liquid interface at the middle of the melt pool bottom, as pointed out in Fig. 6(h). The original X-ray image of Fig. 6(b) without labelling the melt pool boundary was provided in Supplementary Fig. 3 to illustrate the visibility of melt pool solid-liquid interface.

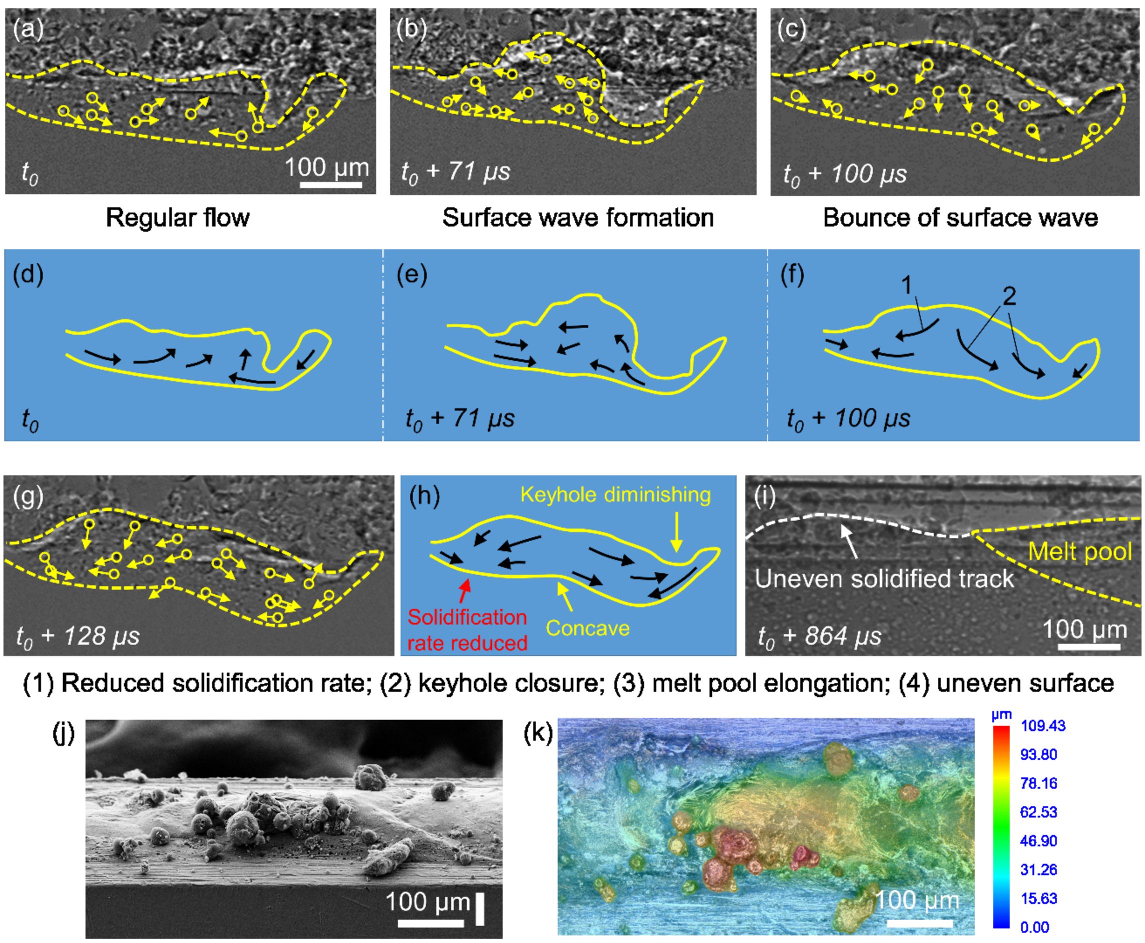

Fig. 6. Significant keyhole oscillation induced global melt flow instability. *The laser power is 312 W with a scan speed of 0.6 m/s. The material is AlSi10Mg. (a–c) X-ray images showing the formation and propagation of an abnormal surface wave. (d–f) Schematic illustration of the melt*

flow pattern in (a–c). (g, i) X-ray images showing the consequences induced by the melt flow instability. (h) Schematic illustration of the melt flow pattern in (g). (j) SEM image of the solidified track in (i). (k) Surface profile of the solidified track in (i) and (j).

(2) The keyhole cavity was filled up by the forward-moving flow, as shown in Fig. 6(g,h), following a similar mechanism as the flow-colliding-induced keyhole closure revealed in Fig. 3(f–h).

(3) The solidification at the tail of the melt pool was delayed by the backward-moving flow, due to the extra mass of molten alloy transported to the rear area. As a result, the melt pool elongated from 605 ± 9 μm to 691 ± 10 μm during the event.

(4) An uneven surface of the solidified track was left when the surface wave reached the tail of the melt pool and solidified with an elevated liquid level, as exhibited in Fig. 6(i,j). The surface roughness is characterized by surface profiling, as shown in Fig. 6(k). The highest point at the uneven solidified track is ~40 μm higher than the average height of the solidified track.

So far, we have revealed the melt flow instabilities induced by powder/droplet impact and significant keyhole oscillation. Their individual effects on various size of melt pools are demonstrated to be different. In brief, the instabilities occurring in a large melt pool tend to influence a portion of the melt pool, while those occurring in a relatively small melt pool usually trigger a global reaction to the whole melt pool and can be more detrimental to the process.

3.3 Melting-mode switching induced melt flow instability

The instabilities unveiled above occur under a single melting mode without melting-mode transition during scanning. However, a distinct type of melt flow instability can be triggered by the switching of melting modes, which is a common yet often overlooked phenomenon due to the difficulties to investigate/recognize by ex-situ examinations.

We observed a melting-mode switching event during a continuous laser scanning of a 100 μm thick AlSi10Mg powder on an AlSi10Mg substrate, with a constant laser power of 312 W and scan speed of 0.6 m/s. Initially, as shown in Fig. 7(a), the melt pool was in conduction mode, where there was no visible keyhole under the laser beam. Indicated by the motion of tracers, the melt flow in the melt pool exhibited a pattern consistent with the literature [23]. However, the melting mode switched into transition mode after 0.5 ms without any change in processing parameters, as shown in Fig. 7(b). By connecting the moving directions of individual tracers, the overall flow pattern in the transition-mode melt pool was mapped out and schematically illustrated in Fig. 7(c). The front-half (keyhole-adjacent region) of the melt pool exhibited a distinct pattern from the conduction-mode flow due to the intensive interruption caused by the keyhole, while the rear-half of the melt pool maintained a similar pattern as the conduction-mode flow. The newly-formed keyhole enhanced the laser absorption [39] and led to an increased melt pool volume. As a result, the melt pool depth increased from 208 ± 10 μm (conduction-mode) to 331 ± 7 μm (transition-mode).

We quantified the 2D flow speed in transition-mode melt pool by evaluating the tracers' speed at four locations, as shown in Fig. 7(c): A—downward flow along the front melt pool bottom; B—upward-forward flow toward the keyhole outlet; C—backward flow along the melt pool surface; and D—forward flow along the rear melt pool bottom. Figure 7(d) displays the average speeds and maximum speeds of the four flows. Flow-A has the highest average speed of 1.96 ± 0.68 m/s and a maximum speed of 3.39 m/s. Flow-D exhibited the lowest average speed of 0.55 ± 0.2 m/s and the lowest maximum speed of 1.14 m/s.

We did not observe a certain frequency (or period) of melting-mode switching during laser scanning. As shown in Supplementary Fig. 4, the melting-mode switching seems to happen occasionally.

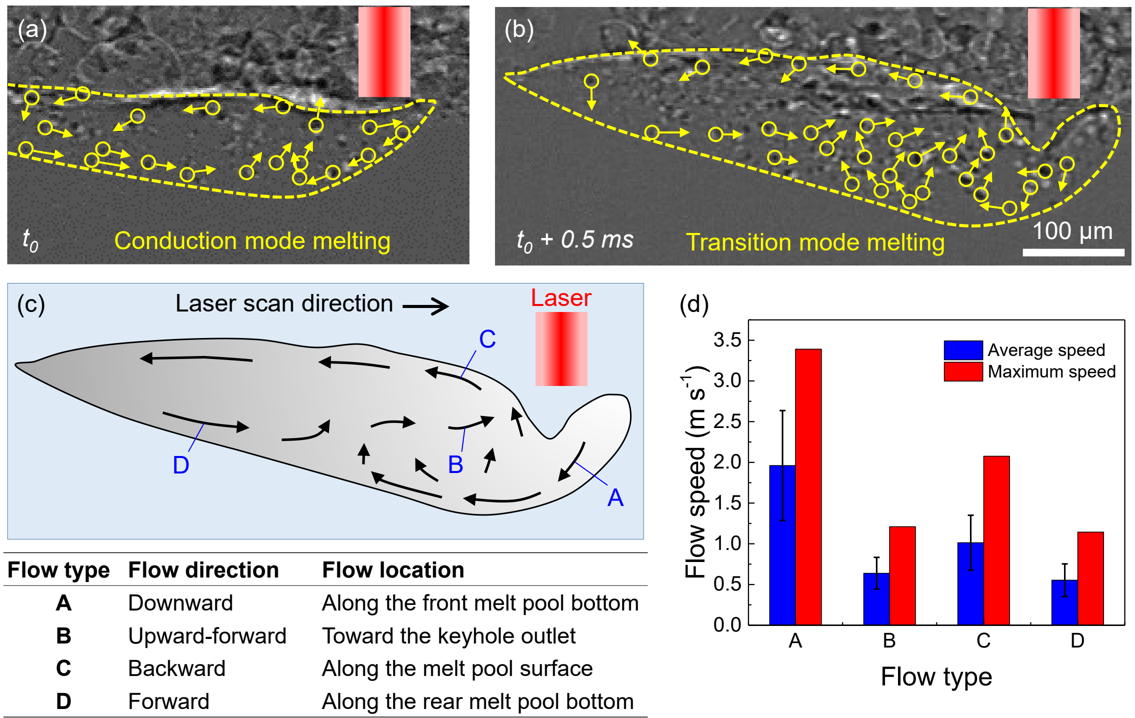

Flow type	Flow direction	Flow location
A	Downward	Along the front melt pool bottom
B	Upward-forward	Toward the keyhole outlet
C	Backward	Along the melt pool surface
D	Forward	Along the rear melt pool bottom

Fig. 7. Melting mode switching induced melt flow instability. *(a, b) X-ray images showing the melt flow change from conduction mode melting to transition mode melting within 0.5 ms. The laser power is 312 W with a scan speed of 0.6 m/s. The material is AlSi10Mg. (c) Schematic illustration of the melt flow pattern in transition mode melt pool (b). (d) Measurement of melt flow speed in transition mode melt pool. Error bars represent standard deviation, $n \geq 21$ independent replicates.*

4. Discussion

4.1 Melt flow evolution among different melting modes

Although the regular melt flow patterns under conduction-mode and keyhole-mode laser melting have been explicitly studied [23–25], it remains unclear how does the melt flow pattern change from a simple flow (conduction-mode flow pattern, Fig. 8(a)) to a complex flow (keyhole-mode flow pattern, Fig. 8(c)). Is such change arbitrary? Or is there a pattern to follow? Here, with the missing-link identified in this work (transition-mode flow pattern), we clarified the complete evolution path of melt flow among different melting modes, as demonstrated in Fig. 8.

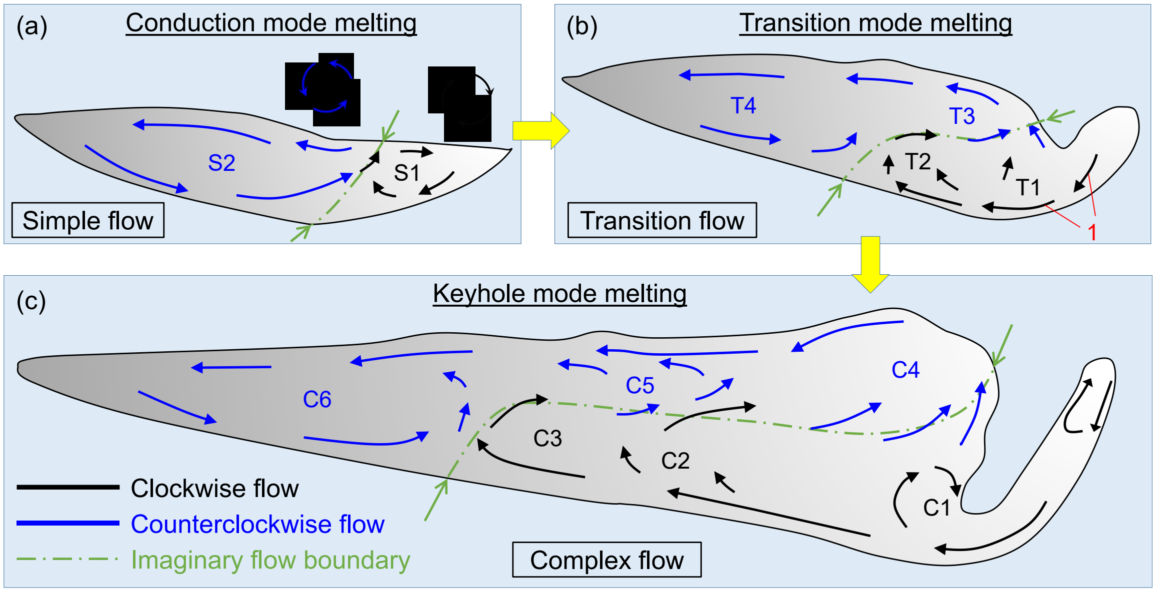

Fig. 8. Melt flow evolution among different melting modes. *(a) Regular melt flow pattern in conduction mode melt pool. (b) Regular melt flow pattern in transition mode melt pool. (c) Regular melt flow pattern in keyhole mode melt pool. Black arrows mark clockwise-moving flow. Blue arrows mark counterclockwise-moving flow. Green line marks the imaginary-boundary of clockwise flow and counterclockwise flow for better interpretation.*

In general, the complexity of the melt flow increases in scale with the melt pool size (or aspect ratio). The simple flow pattern in a conduction-mode melt pool contains two circulations—a clockwise circulation S1 and a counterclockwise circulation S2, as shown in Fig. 8(a). In transition-mode melt pool (Fig. 8(b)), the shallow keyhole exerted extra momentum to the downward flow (flow-1) along the front melt pool boundary, transporting the flow further into the body of melt pool. Compared with the clockwise circulation S1 in the conduction mode, this region was stretched into two clockwise vortices T1 and T2 in transition mode. Similarly, the counterclockwise circulation S2 was also elongated into two partial counterclockwise vortices T3 and T4, as shown in Fig. 8(b). When it comes to keyhole mode, Fig. 8(c), the deep keyhole pushed the clockwise flow deeper into the melt pool. Thus, several vortices, C1, C2, and C3, formed along the path. The counterclockwise region was stretched even longer, partitioned by several counterclockwise flows C4, C5, and C6. Therefore, the melt flow patterns from conduction mode to keyhole mode gain complexity by the expansion of the clockwise region and counterclockwise region, with more vortices forming in each region.

4.2 Mechanisms for significant keyhole oscillation

We have identified keyhole oscillation as an important source for melt flow instabilities. However, the mechanisms for causing significant keyhole oscillation are also various. Previous modelling works have proposed the extra reflection of laser beam within the keyhole as a source for causing keyhole fluctuations [40,41]. The unevenly distribution of laser energy on the keyhole surface was also identified by multi-physics modelling to cause keyhole fluctuations [34]. Experimental work based on in-situ synchrotron imaging has revealed keyhole oscillations could be induced by opposite flows around keyhole, or by the variation of laser absorption on nonuniformly-packed powder bed [42]. It was also reported that the presence of powder could also induce keyhole fluctuations [13], yet no detailed mechanisms were revealed. Here, we report two new powder-based mechanisms for causing significant keyhole oscillations, as shown in Fig. 9.

The first mechanism is laser-blocking induced keyhole oscillation, as demonstrated in Fig. 9(a–e). At stable stage, the laser beam will incident on the front keyhole wall (Fig. 9(a)). However, sometimes the powder agglomerate ahead of the laser and form a large, floating droplet on powder bed[9], as circled by the dashed line in Fig. 9(a). Once the moving laser catch up with the droplet, the laser beam could be partially blocked by the droplet (Fig. 9(b)). The front keyhole wall under the blocked-beam elevated due to the less-intensive vaporization, as shown in the inset of Fig. 9(b), leaving a reduced inclination angle (β) of front keyhole wall as compared with the large inclination angle (α) under regular laser radiation. The overall keyhole size also shrank due to the insufficient laser radiation. In the next moment, Fig. 9(c), the localized vaporization on the droplet pushed the droplet moving along the laser scanning direction and left the laser radiation area. A sudden release of the laser energy to the keyhole promoted the intensive vaporization-induced recoil pressure, which expanded the keyhole cavity rapidly. In this manner, the keyhole completed an oscillation cycle by the laser block-unblock induced keyhole shrinkage-expansion process. The oscillation frequency depends on how often the laser is blocked. For example, we captured two laser-blocking events within 40 μs, as displayed in Fig. 9(b–d). The oscillation amplitude depends on how much of the laser energy is blocked. For example, the keyhole size only shrank when the laser is half-blocked in Fig. 9(b), while the keyhole cavity almost vanished when the laser is nearly fully-blocked in Fig. 9(e).

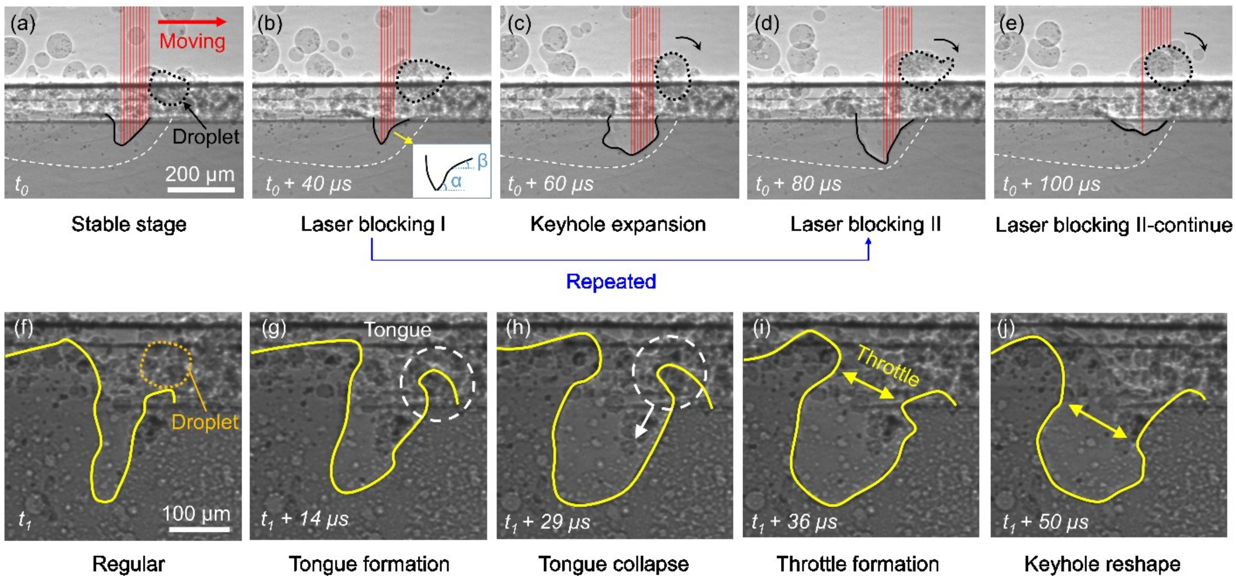

Fig. 9. Mechanisms for causing significant keyhole oscillation. *(a–e) Laser-powder interaction induced significant keyhole oscillation. The laser power is 520 W with a scan speed of 0.4 m/s. The material is Al6061. (f–j) Powder incorporation induced significant keyhole oscillation. The laser power is 364 W with a scan speed of 0.6 m/s. The material is AlSi10Mg.*

The second mechanism is powder-incorporation induced keyhole oscillation, as shown in Fig. 9(f–j). The beginning of this event is similar to the first mechanism, where a floating droplet on powder bed formed ahead of laser beam during laser scanning in Fig. 9(f). However, instead of being pushed away, the droplet was captured by the front rim of the melt pool and formed a "tongue"-shape protrusion (Fig. 9(g)). The tongue then collapsed into the keyhole by moving downward along the front keyhole wall (Fig. 9(h)). The inclined tongue, together with the rear rim of the keyhole, formed a throttle at the keyhole outlet (Fig. 9(j)), which restricted the exhaust of metal vapor and also guided more laser reflection from the front keyhole wall toward the rare keyhole wall [43]. As a result, the keyhole developed into a pocket shape, with an increased width over three times large as the regular keyhole width. The expanded keyhole persists as long as the throttle exists. However, the keyhole profile will keep being reshaped by the throttle displacement, as shown in Fig. 9(j), leading to continuous disturbances to the surrounding area before the throttle fades away.

It should be emphasized that all the observations reported in the present work are the projected information on the 2D imaging plane. Although the selected 2D imaging plane does not account for the out-of-plane (3D) particle movement, the tracer movement within the selected imaging plane can fairly reflect the physics underlying flow instabilities. The reasons being: (1) Statistically, the tracers have more tendency to move within the selected imaging plane rather than moving out of plane, because the melt pool shape in LPBF is usually elongated along the laser scan direction. It has been reported that the melt pool length can be several times larger than the width during LPBF process [4]. (2) The melt flow patterns exhibit more complexity on the selected imaging plane (perpendicular to the X-ray beam) rather than on the plane parallel to the X-ray beam [23].

Therefore, the instabilities we observed on 2D projection plane are valid and not affected by the out-of-plane (3D) particle movements. However, there may be chances that we miss the instability that happens within the plane parallel to the X-ray beam.

5. Conclusion

In the present work, we experimentally revealed the melt flow stabilities in laser metal additive manufacturing process by in-situ high-speed high-resolution synchrotron X-ray imaging. The major conclusions are drawn below:

(1) We identified three mechanisms as the major cause for melt flow instabilities, namely: powder/droplet impact, significant keyhole oscillation, and melting-mode switching. We demonstrated that these instabilities could roughen the part surface finish, break the energy balance within the melt pool (by changing the instant laser absorption), and disturb the solidification process at the melt pool solid-liquid interface.

(2) We unraveled the evolution path of melt flow pattern among different melting modes. The melt pool was found to be separated into a clockwise flow region and a counterclockwise flow region. The elongation of the two regions facilitated the melt pool development from simple flow to complex flow.

(3) We explored two mechanisms for causing significant keyhole oscillation. One mechanism is the laser-blocking induced keyhole oscillation, where powder droplets could occasionally block the laser path and reduce the energy input to the keyhole. The other one is the powder-incorporation induced keyhole oscillation, where the capturing of new particles reshapes the keyhole profile.

The process instability mechanisms revealed in this work provide the foundation for development of processing approaches to mitigate instabilities in laser metal additive manufacturing processes. The melt flow dynamics revealed here are important for the development and validation of high-fidelity computational models.

References

[1] D. Loterie, P. Delrot, C. Moser, High-resolution tomographic volumetric additive manufacturing, Nat. Commun. 11 (2020) 852. https://doi.org/10.1038/s41467-020-14630-4.

[2] J.J. Schwartz, A.J. Boydston, Multimaterial actinic spatial control 3D and 4D printing, Nat. Commun. 10 (2019) 791. https://doi.org/10.1038/s41467-019-08639-7.

[3] B.E. Kelly, I. Bhattacharya, H. Heidari, M. Shusteff, C.M. Spadaccini, H.K. Taylor, Volumetric additive manufacturing via tomographic reconstruction, Science (80-.). 363 (2019) 1075–1079. https://doi.org/10.1126/science.aau7114.

[4] Q. Guo, C. Zhao, M. Qu, L. Xiong, L.I. Escano, S.M.H. Hojjatzadeh, N.D. Parab, K. Fezzaa, W. Everhart, T. Sun, L. Chen, In-situ characterization and quantification of melt pool variation under constant input energy density in laser powder bed fusion additive manufacturing process, Addit. Manuf. 28 (2019) 600–609. https://doi.org/10.1016/j.addma.2019.04.021.

[5] C.L.A. Leung, S. Marussi, R.C. Atwood, M. Towrie, P.J. Withers, P.D. Lee, In situ X-ray imaging of defect and molten pool dynamics in laser additive manufacturing, Nat. Commun. 9 (2018) 1355. https://doi.org/10.1038/s41467-018-03734-7.

[6] S.M.H. Hojjatzadeh, N.D. Parab, W. Yan, Q. Guo, L. Xiong, C. Zhao, M. Qu, L.I. Escano, X. Xiao, K. Fezzaa, W. Everhart, T. Sun, L. Chen, Pore elimination mechanisms during 3D printing of metals, Nat. Commun. 10 (2019) 3088. https://doi.org/10.1038/s41467-019-10973-9.

[7] A.A. Martin, N.P. Calta, S.A. Khairallah, J. Wang, P.J. Depond, A.Y. Fong, V. Thampy, G.M. Guss, A.M. Kiss, K.H. Stone, C.J. Tassone, J. Nelson Weker, M.F. Toney, T. van Buuren, M.J. Matthews, Dynamics of pore formation during laser powder bed fusion additive manufacturing, Nat. Commun. 10 (2019) 1987. https://doi.org/10.1038/s41467-019-10009-2.

[8] J.-B. Forien, N.P. Calta, P.J. DePond, G.M. Guss, T.T. Roehling, M.J. Matthews, Detecting keyhole pore defects and monitoring process signatures during laser powder bed fusion: A correlation between in situ pyrometry and ex situ X-ray radiography, Addit. Manuf. 35 (2020) 101336. https://doi.org/10.1016/j.addma.2020.101336.

[9] Z.A. Young, Q. Guo, N.D. Parab, C. Zhao, M. Qu, L.I. Escano, K. Fezzaa, W. Everhart, T. Sun, L. Chen, Types of spatter and their features and formation mechanisms in laser powder bed fusion additive manufacturing process, Addit. Manuf. 36 (2020) 101438. https://doi.org/10.1016/j.addma.2020.101438.

[10] Q. Guo, C. Zhao, L.I. Escano, Z. Young, L. Xiong, K. Fezzaa, W. Everhart, B. Brown, T.

Sun, L. Chen, Transient dynamics of powder spattering in laser powder bed fusion additive manufacturing process revealed by in-situ high-speed high-energy x-ray imaging, Acta Mater. 151 (2018) 169–180. https://doi.org/10.1016/j.actamat.2018.03.036.

[11] S.A. Khairallah, T. Sun, B.J. Simonds, Onset of periodic oscillations as a precursor of a transition to pore-generating turbulence in laser melting, Addit. Manuf. Lett. 1 (2021) 100002. https://doi.org/10.1016/j.addlet.2021.100002.

[12] C. Zhao, N.D. Parab, X. Li, K. Fezzaa, W. Tan, A.D. Rollett, T. Sun, Critical instability at moving keyhole tip generates porosity in laser melting, Science (80-.). 370 (2020) 1080–1086. https://doi.org/10.1126/science.abd1587.

[13] R. Cunningham, C. Zhao, N. Parab, C. Kantzos, J. Pauza, K. Fezzaa, T. Sun, A.D. Rollett, Keyhole threshold and morphology in laser melting revealed by ultrahigh-speed x-ray imaging, Science (80-.). 363 (2019) 849–852. https://doi.org/10.1126/science.aav4687.

[14] M. Colopi, A.G. Demir, L. Caprio, B. Previtali, Limits and solutions in processing pure Cu via selective laser melting using a high-power single-mode fiber laser, Int. J. Adv. Manuf. Technol. 104 (2019) 2473–2486. https://doi.org/10.1007/s00170-019-04015-3.

[15] L. Scime, J. Beuth, Using machine learning to identify in-situ melt pool signatures indicative of flaw formation in a laser powder bed fusion additive manufacturing process, Addit. Manuf. 25 (2019) 151–165. https://doi.org/10.1016/j.addma.2018.11.010.

[16] M. Grasso, A.G. Demir, B. Previtali, B.M. Colosimo, In situ monitoring of selective laser melting of zinc powder via infrared imaging of the process plume, Robot. Comput. Integr. Manuf. 49 (2018) 229–239. https://doi.org/10.1016/j.rcim.2017.07.001.

[17] V. Gunenthiram, P. Peyre, M. Schneider, M. Dal, F. Coste, R. Fabbro, Analysis of laser–melt pool–powder bed interaction during the selective laser melting of a stainless steel, J. Laser Appl. 29 (2017) 022303. https://doi.org/10.2351/1.4983259.

[18] S. Wang, L. Zhu, Y. Dun, Z. Yang, J.Y.H. Fuh, W. Yan, Multi-physics modeling of direct energy deposition process of thin-walled structures: defect analysis, Comput. Mech. 67 (2021) 1229–1242. https://doi.org/10.1007/s00466-021-01992-9.

[19] W. Ren, Z. Zhang, Y. Lu, G. Wen, J. Mazumder, In-situ monitoring of laser additive manufacturing for Al7075 alloy using emission spectroscopy and plume imaging, IEEE Access. 9 (2021) 61671–61679. https://doi.org/10.1109/ACCESS.2021.3074703.

[20] Y. Zhao, Y. Koizumi, K. Aoyagi, D. Wei, K. Yamanaka, A. Chiba, Molten pool behavior and effect of fluid flow on solidification conditions in selective electron beam melting (SEBM) of a biomedical Co-Cr-Mo alloy, Addit. Manuf. 26 (2019) 202–214. https://doi.org/10.1016/j.addma.2018.12.002.

[21] M. Bisht, N. Ray, F. Verbist, S. Coeck, Correlation of selective laser melting-melt pool events with the tensile properties of Ti-6Al-4V ELI processed by laser powder bed fusion, Addit. Manuf. 22 (2018) 302–306. https://doi.org/10.1016/j.addma.2018.05.004.

[22] K.G. Prashanth, J. Eckert, Formation of metastable cellular microstructures in selective laser melted alloys, J. Alloys Compd. 707 (2017) 27–34. https://doi.org/10.1016/j.jallcom.2016.12.209.

[23] Q. Guo, C. Zhao, M. Qu, L. Xiong, S.M.H. Hojjatzadeh, L.I. Escano, N.D. Parab, K. Fezzaa, T. Sun, L. Chen, In-situ full-field mapping of melt flow dynamics in laser metal additive manufacturing, Addit. Manuf. 31 (2020) 100939. https://doi.org/10.1016/j.addma.2019.100939.

[24] L. Aucott, H. Dong, W. Mirihanage, R. Atwood, A. Kidess, S. Gao, S. Wen, J. Marsden, S. Feng, M. Tong, T. Connolley, M. Drakopoulos, C.R. Kleijn, I.M. Richardson, D.J. Browne, R.H. Mathiesen, H. V Atkinson, Revealing internal flow behaviour in arc welding and additive manufacturing of metals, Nat. Commun. 9 (2018) 5414. https://doi.org/10.1038/s41467-018-07900-9.

[25] S.J. Clark, C.L.A. Leung, Y. Chen, L. Sinclair, S. Marussi, P.D. Lee, Capturing Marangoni flow via synchrotron imaging of selective laser melting, IOP Conf. Ser. Mater. Sci. Eng. 861 (2020) 012010. https://doi.org/10.1088/1757-899X/861/1/012010.

[26] S.J. Wolff, H. Wang, B. Gould, N. Parab, Z. Wu, C. Zhao, A. Greco, T. Sun, In situ X-ray imaging of pore formation mechanisms and dynamics in laser powder-blown directed energy deposition additive manufacturing, Int. J. Mach. Tools Manuf. 166 (2021) 103743. https://doi.org/10.1016/j.ijmachtools.2021.103743.

[27] A. Bobel, L.G. Hector, I. Chelladurai, A.K. Sachdev, T. Brown, W.A. Poling, R. Kubic, B. Gould, C. Zhao, N. Parab, A. Greco, T. Sun, In situ synchrotron X-ray imaging of 4140 steel laser powder bed fusion, Materialia. 6 (2019) 100306. https://doi.org/10.1016/j.mtla.2019.100306.

[28] C. Qiu, C. Panwisawas, M. Ward, H.C. Basoalto, J.W. Brooks, M.M. Attallah, On the role of melt flow into the surface structure and porosity development during selective laser melting, Acta Mater. 96 (2015) 72–79. https://doi.org/10.1016/j.actamat.2015.06.004.

[29] S.M.H. Hojjatzadeh, N.D. Parab, Q. Guo, M. Qu, L. Xiong, C. Zhao, L.I. Escano, K. Fezzaa, W. Everhart, T. Sun, L. Chen, Direct observation of pore formation mechanisms during LPBF additive manufacturing process and high energy density laser welding, Int. J. Mach. Tools Manuf. 153 (2020) 103555. https://doi.org/10.1016/j.ijmachtools.2020.103555.

[30] M. Xia, D. Gu, G. Yu, D. Dai, H. Chen, Q. Shi, Influence of hatch spacing on heat and mass transfer, thermodynamics and laser processability during additive manufacturing of Inconel 718 alloy, Int. J. Mach. Tools Manuf. 109 (2016) 147–157. https://doi.org/10.1016/j.ijmachtools.2016.07.010.

[31] D. Dai, D. Gu, Influence of thermodynamics within molten pool on migration and distribution state of reinforcement during selective laser melting of AlN/AlSi10Mg composites, Int. J. Mach. Tools Manuf. 100 (2016) 14–24. https://doi.org/10.1016/j.ijmachtools.2015.10.004.

[32] D. Gu, M. Xia, D. Dai, On the role of powder flow behavior in fluid thermodynamics and laser processability of Ni-based composites by selective laser melting, Int. J. Mach. Tools Manuf. 137 (2019) 67–78. https://doi.org/10.1016/j.ijmachtools.2018.10.006.

[33] S.A. Khairallah, A.T. Anderson, A. Rubenchik, W.E. King, Laser powder-bed fusion additive manufacturing: Physics of complex melt flow and formation mechanisms of

pores, spatter, and denudation zones, Acta Mater. 108 (2016) 36–45. https://doi.org/10.1016/j.actamat.2016.02.014.

[34] L. Wang, Y. Zhang, H.Y. Chia, W. Yan, Mechanism of keyhole pore formation in metal additive manufacturing, Npj Comput. Mater. 8 (2022) 22. https://doi.org/10.1038/s41524-022-00699-6.

[35] S. Ly, A.M. Rubenchik, S.A. Khairallah, G. Guss, M.J. Matthews, Metal vapor micro-jet controls material redistribution in laser powder bed fusion additive manufacturing, Sci. Rep. 7 (2017) 4085. https://doi.org/10.1038/s41598-017-04237-z.

[36] T.B. Sercombe, X. Li, Selective laser melting of aluminium and aluminium metal matrix composites: review, Mater. Technol. 31 (2016) 77–85. https://doi.org/10.1179/1753555715Y.0000000078.

[37] M. Bayat, A. Thanki, S. Mohanty, A. Witvrouw, S. Yang, J. Thorborg, N.S. Tiedje, J.H. Hattel, Keyhole-induced porosities in Laser-based Powder Bed Fusion (L-PBF) of Ti6Al4V: High-fidelity modelling and experimental validation, Addit. Manuf. 30 (2019) 100835. https://doi.org/10.1016/j.addma.2019.100835.

[38] T.-N. Le, Y.-L. Lo, Effects of sulfur concentration and Marangoni convection on melt-pool formation in transition mode of selective laser melting process, Mater. Des. 179 (2019) 107866. https://doi.org/10.1016/j.matdes.2019.107866.

[39] M. Matthews, J. Trapp, G. Guss, A. Rubenchik, Direct measurements of laser absorptivity during metal melt pool formation associated with powder bed fusion additive manufacturing processes, J. Laser Appl. 30 (2018) 032302. https://doi.org/10.2351/1.5040636.

[40] A.A. Martin, N.P. Calta, J.A. Hammons, S.A. Khairallah, M.H. Nielsen, R.M. Shuttlesworth, N. Sinclair, M.J. Matthews, J.R. Jeffries, T.M. Willey, J.R.I. Lee, Ultrafast dynamics of laser-metal interactions in additive manufacturing alloys captured by in situ X-ray imaging, Mater. Today Adv. 1 (2019) 100002. https://doi.org/https://doi.org/10.1016/j.mtadv.2019.01.001.

[41] N. Kouraytem, X. Li, R. Cunningham, C. Zhao, N. Parab, T. Sun, A.D. Rollett, A.D. Spear, W. Tan, Effect of laser-matter interaction on molten pool flow and keyhole dynamics, Phys. Rev. Appl. 11 (2019) 064054. https://doi.org/10.1103/PhysRevApplied.11.064054.

[42] Y. Chen, S.J. Clark, C.L.A. Leung, L. Sinclair, S. Marussi, M.P. Olbinado, E. Boller, A. Rack, I. Todd, P.D. Lee, In-situ Synchrotron imaging of keyhole mode multi-layer laser powder bed fusion additive manufacturing, Appl. Mater. Today. 20 (2020) 100650. https://doi.org/10.1016/j.apmt.2020.100650.

[43] L. Wang, Y. Zhang, W. Yan, Evaporation Model for Keyhole Dynamics During Additive Manufacturing of Metal, Phys. Rev. Appl. 14 (2020) 064039. https://doi.org/10.1103/PhysRevApplied.14.064039.